Design of Semiconducting Tetrahedral $Mn_{1-x}Zn_xO$ Alloys and Their Application to Solar Water Splitting

Haowei Peng, Paul F. Ndione, David S. Ginley, Andriy Zakutayev, and Stephan Lany

National Renewable Energy Laboratory, 15013 Denver West Parkway, Golden, Colorado 80401, USA

(Received 22 July 2014; revised manuscript received 27 February 2015; published 18 May 2015)

Transition metal oxides play important roles as contact and electrode materials, but their use as active layers in solar energy conversion requires achieving semiconducting properties akin to those of conventional semiconductors like Si or GaAs. In particular, efficient bipolar carrier transport is a challenge in these materials. Based on the prediction that a tetrahedral polymorph of MnO should have such desirable semiconducting properties, and the possibility to overcome thermodynamic solubility limits by non-equilibrium thin-film growth, we exploit both structure-property and composition-structure relationships to design and realize novel wurtzite-structure $Mn_{1-x}Zn_xO$ alloys. At Zn compositions above $x \approx 0.3$, thin films of these alloys assume the tetrahedral wurtzite structure instead of the octahedral rocksalt structure of MnO, thereby enabling semiconductor properties that are unique among transition metal oxides, i.e., a band gap within the visible spectrum, a band-transport mechanism for both electron and hole carriers, electron doping, and a band lineup suitable for solar hydrogen generation. A proof of principle is provided by initial photo-electrocatalytic device measurements, corroborating, in particular, the predicted favorable hole-transport properties of these alloys.

DOI: 10.1103/PhysRevX.5.021016

Subject Areas: Condensed Matter Physics, Energy Research, Semiconductor Physics

I. INTRODUCTION

Inorganic semiconductor applications, including microelectronics, light-emitting diodes, and photovoltaics, are mainly based on tetrahedrally coordinated semiconductor materials whose structure is derived from the diamond lattice, i.e., Si and III-V (e.g., GaAs) or II-VI (e.g., CdTe) compounds [1]. In most oxides, on the other hand, the cations prefer octahedral coordination, and only a few oxides are known to have similarly favorable semiconducting properties. This observation suggests that the manipulation of the coordination symmetry could be exploited to create novel semiconducting oxides, in the pursuit of the grand challenge to design new forms of matter with tailored properties [2]. Indeed, ZnO, which is one of the few tetrahedrally coordinated oxides, is a prototypical wide-gap semiconductor oxide with good transport and optical properties and is used for numerous applications [3]. In many transition metal oxides, however, the self-trapping of electron or hole carriers leads to an unfavorable small-polaron mechanism [4] and to poor mobilities. Additionally, many such oxides resist the introduction of such carriers via doping by self-compensation mechanisms [5], and many have too large band gaps to overlap the optical absorption with the solar spectrum. Overcoming all of these issues simultaneously is necessary for eventual application of such materials as solar absorbers or photo-anode materials for photo-electrochemical water splitting [6,7].

Our recent computational research on d^5 oxides has predicted that a metastable zinc-blende (ZB) polymorph of MnO should have a much smaller band gap and a favorable bandlike hole transport mechanism, compared to the rocksalt (RS) ground-state structure [8]. Thus, stabilizing the tetrahedral over the usual octahedral coordination of Mn(II) could be instrumental to achieve semiconducting Mn oxides. The hexagonal wurtzite (WZ) structure of MnO has recently been realized by growth on a carbon template [9], indicating that tetrahedrally bonded Mn(II) is energetically feasible. An alternative strategy, pursued in the present work, is stabilizing tetrahedral Mn(II) by alloying with ZnO. There is a body of literature on thin-film growth of Mn-doped ZnO by pulsed laser deposition, and $Mn_{1-x}Zn_xO$ alloys in the Zn-rich composition range have attracted much interest as diluted magnetic oxides, with focus on the magnetic properties of Mn impurities in ZnO [10]. However, there are no experimental reports of alloys in the Mn-rich composition range, where the structural transition between the octahedral rocksalt structure (MnO ground state) and the tetrahedral wurtzite structure (ZnO ground state) is expected [11], and previous theoretical investigations for such alloys were restricted to the RS

Published by the American Physical Society under the terms of the Creative Commons Attribution 3.0 License. Further distribution of this work must maintain attribution to the author(s) and the published article's title, journal citation, and DOI.

structure [12,13]. The alloy composition range of interest lies inside the miscibility gap [14], and the properties of such alloys are unknown.

In the present study, we exploit both structure-property and composition-structure relationships to design and realize novel semiconducting transition metal oxides by *heterostructural alloying* of the binary oxides MnO and ZnO. We use *ab initio* electronic structure methods to predict, for these $Mn_{1-x}Zn_xO$ alloys, the transition from the octahedral rocksalt into the tetrahedral WZ structure, the equilibrium phase diagram, the band-structure and optical properties, the hole self-trapping energies, as well as the surface ionization potentials, which provide a good estimate for the band lineup with respect to the redox potentials for solar water splitting [15]. Utilizing the possibility to overcome thermodynamic solubility limits by nonequilibrium growth [16], we use combinatorial pulsed laser deposition (PLD) to grow $Mn_{1-x}Zn_xO$ thin-film samples in the composition range $0.05 \leq x \leq 0.75$, and determine the nonequilibrium phase diagram for metastable RS/WZ single-phase compositions in the PLD growth. We note that such nonequilibrium growth of thin films becomes increasingly instrumental for the control of materials properties, e.g., the conductivity on ZnO-based transparent conducting oxides [17]. We further characterize the optical absorption as a function of composition and demonstrate electron doping using Ga dopants. Finally, we present initial results of photo-electrocatalytic (PEC) measurements on devices based on $Mn_{0.5}Zn_{0.5}O$ alloys, which provide a proof of concept and, in particular, corroborate the predicted favorable carrier transport properties. This article is structured to present computational and experimental results in an integrated way, addressing the equilibrium and nonequilibrium phase diagrams (Sec. II, Fig. 1), band gaps and optical properties (Sec. III, Fig. 2), transport properties and doping (Sec. IV, Table I, and Fig. 3), as well as the band lineup relative to vacuum (Sec. V, Fig. 4). Initial results of PEC characterization of devices based on $Mn_{0.5}Zn_{0.5}O$ alloys are presented in Sec. VI (Fig. 5), and a detailed account of these experiments will be presented elsewhere [18]. Details on the computational and experimental methods, as well as some supplementary material, are appended at the end of this article (see the Appendix, Figs. 6–9).

II. EQUILIBRIUM AND NONEQUILIBRIUM PHASE DIAGRAMS

Figure 1(a) shows the calculated mixing enthalpy ΔH_m for the $Mn_{1-x}Zn_xO$ alloys as a function of the composition x. For either structure (str = RS, WZ), the mixing enthalpies can be expressed in the form

$$\Delta H_m^{str}(x) = (1-x)\cdot\Delta H_{MnO}^{str} + x\cdot\Delta H_{ZnO}^{str} + \Omega^{str}\cdot x(1-x) \quad (1)$$

with the regular solution interaction parameters $\Omega^{RS} = 46$ and $\Omega^{WZ} = 94$ meV. The interaction parameters were determined from density functional theory (DFT) calculations of alloy models (see also Appendix A 1), and the polymorphic energy ordering ($\Delta H_{ZnO}^{WZ} = +131$ and $\Delta H_{ZnO}^{RS} = +239$ meV) is taken from recent total energy calculations in the random phase approximation (RPA), which were able to overcome inaccuracies of DFT functionals to predict the relative stabilities of the two structures [11]. Above the critical concentration of $x_{RS/WZ} = 0.38$, the WZ structure has a lower enthalpy than RS and would be the energetically preferred structure for a homogeneous alloy. However, the magnitude of the mixing enthalpy implies the existence of a wide miscibility gap.

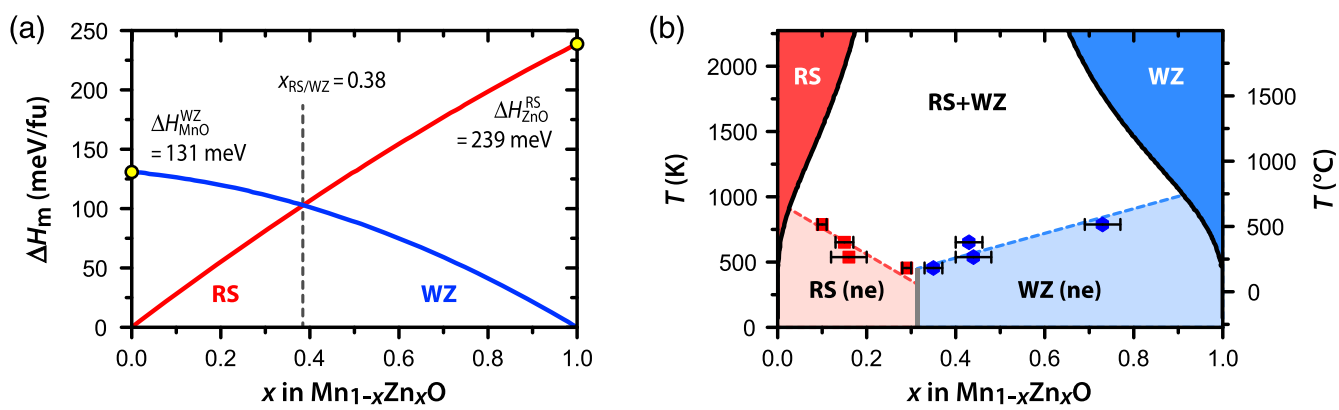

FIG. 1. Mixing enthalpies and phase diagrams for $Mn_{1-x}Zn_xO$ alloys: (a) The calculated mixing enthalpy ΔH_m per formula unit (fu) of the $Mn_{1-x}Zn_xO$ alloy in the RS and WZ structure, as a function of the composition x. (b) The temperature-composition phase diagram of $Mn_{1-x}Zn_xO$. Solid lines are determined from the calculated mixing enthalpy ΔH_m and show the binodal lines separating the RS (dark red) phase, the miscibility gap (white), and the WZ phase (dark blue). The data points show the experimental phase boundaries delineating the nonequilibrium (ne) single-phase regions for PLD growth (dashed lines and light red or blue areas), obtained by the disappearing phase method.

In Fig. 1(b), the temperature vs. composition phase diagram (binodal curve) is shown as determined from the standard common tangent construction in the free-energy $\Delta G(x) = \Delta H(x) - TS(x)$ diagram, using the configurational entropy $S = -k_B[x\ln(x) + (1-x)\ln(1-x)]$ of the random alloy. The finding of a wide and asymmetric miscibility gap, with a larger Mn solubility in ZnO and a smaller Zn solubility in MnO, agrees with experimental solubility measurements [14]. Above 600 °C, the calculated solubilities are, however, smaller than those determined in Ref. [14] at respective temperatures. We note that vibrational entropy contributions, not considered here, often increase the solubility at higher temperatures [19]. However, here we are interested in low-temperature deposition conditions where metastable alloy compositions are stabilized by the kinetic limitation of the phase separation process via diffusion and nucleation of precipitates. Clearly, the targeted composition range around $0.4 < x < 0.5$, where the tetrahedral WZ structure is stable but where MnO is still the majority compound, lies deep inside the miscibility gap [Fig. 1(b)], requiring a nonequilibrium growth technique.

The combinatorial synthesis and characterization approach [20,21] was used to deposit $Mn_{1-x}Zn_xO$ thin-film "libraries" with both a composition [22] and a temperature [23] gradient. The samples of the present work were grown by PLD from MnO and ZnO targets in the temperature range $180\,°C \leq T \leq 520\,°C$, spanning a wide composition range of about $0.05 \leq x \leq 0.75$, which extends to both sides of the predicted critical composition for the structural transition. The RS and WZ phase boundaries were determined from x-ray diffraction (XRD) and x-ray fluorescence (XRF) using the disappearing phase method [24]; i.e., the integrated XRD intensities of the WZ phase were determined over a range of $Mn_{1-x}Zn_xO$ compositions and then extrapolated to zero intensity to determine the solubility of ZnO in the RS structure and, analogously, the solubility of MnO in the WZ structure. The XRD data used to perform this analysis is shown in Fig. 8 (Appendix A 6) for the representative deposition temperature of 297 °C. The two temperature-dependent phase boundaries shown in Fig. 1(b) delineate the RS and WZ single-phase regions from the mixed-phase RS + WZ region, thereby representing a "nonequilibrium phase diagram" for thin-film growth in the present PLD setup. At the lowest deposition temperatures around 180 °C, the RS and WZ phase boundaries approach each other at $x = 0.29$ and 0.35, respectively [see Fig. 1(b)], indicating that the critical composition for the structure transition lies slightly below the theoretically predicted one [$x_{RS/WZ} = 0.38$, cf. Fig. 1(a)].

In the present PLD setup, we achieved essentially complete miscibility at a growth temperature of about 200 °C. With increasing deposition temperature, a miscibility gap opens and the nonequilibrium phase map merges with the equilibrium phase diagram at temperatures above 700 °C [Fig. 1(b)]. An interesting aspect of the present case of heterostructural alloys is that the critical temperatures for binodal and spinodal decomposition are different, in contrast to the more usual situation of an isostructural alloy. Indeed, the spinodal line does not depend on the absolute magnitude of the mixing enthalpy but only on the curvature of $\Delta H_m(x)$. From the calculated interaction parameter $\Omega^{WZ} = 94$ meV, we find that there is no thermodynamic driving force for spinodal decomposition above 270 °C. Thus, alloys grown above this temperature should exhibit a fairly homogeneous cation distribution, as long as the (binodal) phase separation can be kinetically suppressed.

III. BAND GAPS AND OPTICAL PROPERTIES

In order to predict the band gap of the wurtzite $Mn_{1-x}Zn_xO$ alloys, we performed quasiparticle energy band-structure calculations within the GW approximation [25,26] for random-alloy supercell models at the compositions $x = 0.25$, 0.5, and 0.75. The band gaps of the binary end compounds RS-MnO and WZ-ZnO were calculated before as 3.36 eV [8] and 3.29 eV [27], respectively, using the same method. Since the substitutional Mn_{Zn} defect creates an occupied defect state inside the band gap of ZnO [28], we performed additionally a GW defect calculation for an isolated substitutional Mn_{Zn} defect in a ZnO supercell, finding that the top of the Mn-induced impurity band lies 0.45 eV above the valence band maximum (VBM) of ZnO in the dilute ($x \to 1$) limit. Thus, the band gap of Mn-doped ZnO (ZnO:Mn) is reduced by the same amount compared to pure ZnO, i.e., $E_g^{ZnO:Mn} = 2.84$ eV. (Note that here we follow the convention to take the highest occupied state as the VBM, which implies that the band gap of ZnO changes discontinuously upon Mn doping.) From a fit to quadratic order,

$$E_g(x) = (1-x)\cdot E_g^{WZ\text{-}MnO} + x\cdot E_g^{ZnO:Mn} + b\cdot x(1-x), \tag{2}$$

we obtain the composition dependence with a bowing parameter $b = -1.46$ eV. The bowing of the individual band edges and the position of the Mn impurity band in the Zn-rich limit are shown graphically in Fig. 4. The band gap of the $Mn_{1-x}Zn_xO$ alloy at the $x = 0.5$ composition was calculated as 2.30 eV, which is more than 1 eV smaller than either of the band gaps of the end compounds, RS-MnO and WZ-ZnO. However, rather than indicating giant bowing effects, the band-gap reduction stems largely from the large difference between the band gaps of MnO in the normal RS structure (3.36 eV) and in the WZ structure (2.38 eV).

The magnitude of the band gap, i.e., the difference of the quasiparticle energies for electron addition and removal (electron affinity and ionization potential), by itself does not specify whether the absorption is strong enough for

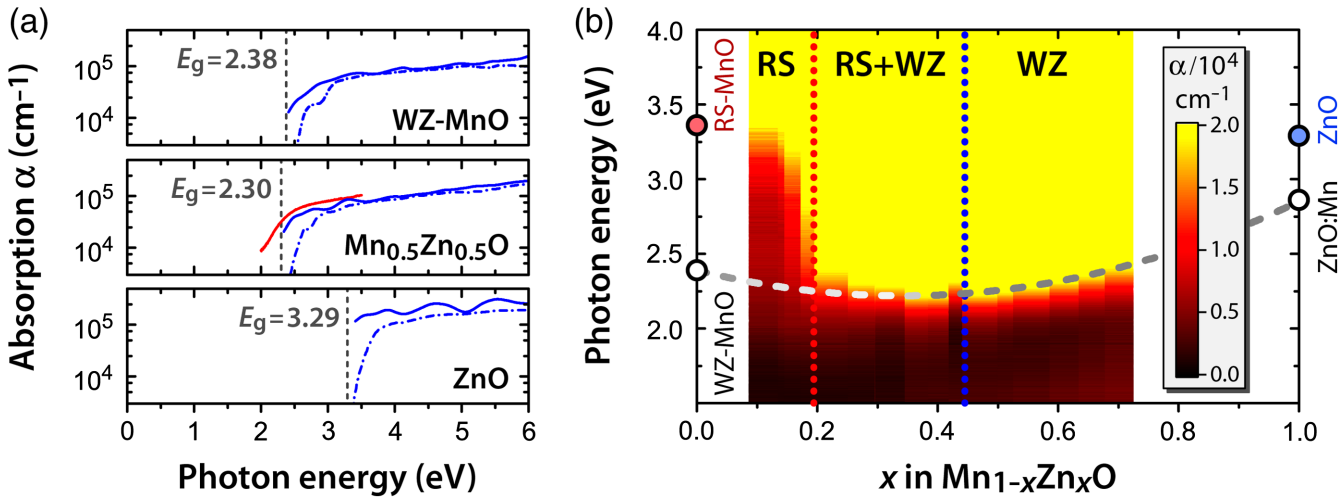

FIG. 2. Band gaps and optical properties: (a) Calculated band gaps (vertical dashed lines) and absorption spectra for wurtzite structure MnO, the $Mn_{0.5}Zn_{0.5}O$ alloy, and ZnO. The spectra are shown for the independent-particle approximation (dash-dotted line) and including electron-hole interactions (solid blue line). For comparison, the experimental absorption spectrum is also shown for the $x = 0.5$ composition (solid red line). (b) The experimental absorption coefficients as a function of composition x and photon energy. The single-phase boundaries for the growth temperature of 297 °C [dotted lines, cf. Fig. 1(b)] and the predicted band-gap energies [dashed line, cf. Eq. (2)] are also shown.

solar-energy applications. Therefore, we calculated, based on the GW band-structure energies, the frequency-dependent dielectric function both within the independent particle approximation and including excitonic effects via time-dependent density functional theory using a hybrid functional kernel [29] (see also Appendix A 1). The resulting optical absorption spectra are shown in Fig. 2(a) (note that phonon-assisted indirect transitions are not included). We observe a direct character for all cases (WZ-MnO, ZnO, and the alloy), in the sense that the absorption onset coincides with the band gap. This behavior is different in RS-MnO, where the band gap is indirect, and where the onset of vertical absorption occurs about 0.5 eV above the gap [8]. The absolute magnitude of the absorption coefficient calculated for $Mn_{0.5}Zn_{0.5}O$ is larger than 4×10^4 cm^{-1} at energies higher than 0.2 eV above the band gap, suggesting that these alloys should be efficient light absorbers even as thin films with thicknesses of 1 μm or less.

Figure 2(b) shows the experimental optical characterization obtained by spatially resolved measurements of the thin-film $Mn_{1-x}Zn_xO$ library grown at a temperature of $T = 297$ °C. Comparing the predicted and measured optical properties for the $Mn_{1-x}Zn_xO$ alloys, we see in Fig. 2(b) that the measured absorption edge (contour plot) lies close to the calculated band gap (dashed line) for compositions of $x \geq 0.2$, where wurtzite-structure crystallites are present, indicating that band-to-band transitions dominate the optical absorption. This characteristic is important for solar absorber materials since other absorption channels such as internal *d*-*d* transitions [30] may not generate electron-hole pairs. At the composition $x = 0.5$, the experimentally measured absorption coefficients agree well with the predictions [cf. Fig. 2(a)], and the Tauc analysis is consistent with a direct allowed band gap of 2.3 eV, while a certain level of absorption remains present at subgap energies (see Fig. 9 in Appendix A 6). At the RS phase boundary $x = 0.19$, the absorption edge shows a discontinuous behavior changing from about 3.3 eV to 2.3 eV, thereby corroborating the structural origin (tetrahedral vs. octahedral coordination) of the band-gap reduction. Thus, the structural modification of MnO via alloying is the enabling mechanism for creating an overlap between the absorption and solar spectra that is suitable for solar-energy harvesting.

IV. TRANSPORT PROPERTIES AND DOPING

Most semiconductor applications require doping with either electron or hole carriers, or even both. In the case of photo-anode materials for photo-electrochemical water-splitting, the solar absorber materials should be *n*-type (electron-carrier) doped, and the minority (hole) carriers should have a long lifetime and a high mobility. From the GW band-structure calculations, we obtained the effective masses for the charge carriers. For the $x = 0.50$ composition ($Mn_{0.5}Zn_{0.5}O$ alloy), we determined an effective electron mass of $m_e^* = 0.30\ m_0$, close to the value of 0.26 calculated for ZnO, which is a prototypical electron conducting oxide with an exceptionally low effective mass [31]. The respective hole mass of $m_h^*/m_0 = 5.6$ is comparable to that of ZnO($m_h^*/m_0 = 3.2$) and is among the smallest values found for oxide semiconductors [8]. (Note that these values represent the density-of-states effective mass for holes, which, because of the degeneracies in the valence band, is larger than the average band effective

mass.) Thus, the band-structure properties are quite favorable for both electron and hole transport.

In order to assess the transport properties, it is, however, necessary to consider polaronic effects. While the large-polaron (Fröhlich) conduction [32] leads to a renormalization of the band effective mass, it still maintains bandlike transport properties. In contrast, the small (Holstein) polaron [33] is a "self-trapped" state in which the carrier (electron or hole) is localized at one or a few atoms, and which can often be associated with a change of the oxidation state of a particular ion. Small-polaron hopping transport is generally characterized by low mobilities, usually assumed to be $\mu \ll 0.1\ \mathrm{cm}^2/\mathrm{Vs}$ ("Bosman–van Daal limit") [4]. A recent study on the polaron hopping transport in RS structure MnO-ZnO alloys [13] found sizable energy barriers around 0.5 eV, suggesting hole mobilities below $10^{-6}\ \mathrm{cm}^2/\mathrm{Vs}$ at room temperature. In the context of solar absorber materials, an important additional implication is that the small polaron creates a deep defect state inside the band gap that acts as a detrimental recombination center [8]. Employing the *ab initio* theory for small-polaron binding energies of Refs. [34,35], we previously investigated how the transport mechanisms for electrons and holes depend on the structure of MnO [8]. Owing to the highly dispersive, *s*-like conduction band [8,36], electrons exhibit bandlike transport similar to in ZnO, irrespective of the structure. The feature of a dispersive conduction band was also recently found for ternary Mn(II) oxides [31]. Thus, electron transport in MnO-ZnO alloys should be described as large-polaron band conduction and not as small-polaron hopping conduction [13]. For hole carriers, the transport mechanism depends on the structure: In the octahedral coordination environment of RS MnO, the small-polaron formation is exothermic, i.e., the self-trapping energy E_{ST} for the process $\mathrm{Mn}^{+\mathrm{II}} + h^+ \rightarrow \mathrm{Mn}^{+\mathrm{III}}$ is negative (here, h^+ denotes a positively charged hole carrier at the VBM). However, in the hypothetical zinc-blende structure of MnO, the small-polaron formation was found to be suppressed because of the tetrahedral coordination [8], which motivated studies on ternary wide-gap Mn(II) oxides with tetrahedral Mn coordination [37,38].

For the purpose of the present work, we performed calculations of the small-polaron binding energy for MnZnO alloys and for ZnO. Within the approach described in Refs. [39,40], the so-called "delocalization error" of DFT [41] is corrected via an additional potential term, which supports the localization of a carrier but which is constructed to preserve the description of the underlying DFT (or hybrid) functional in the absence of a localized carrier (see also Appendix A 3). Since the strength of the potential is determined by a physically motivated quasiparticle energy condition ("Koopmans condition" for electron addition or removal), there are no adjustable parameters and the *ab initio* character is preserved in this approach for calculating small-polaron binding energies. The self-trapping energy of a $\mathrm{Mn}^{+\mathrm{III}}$ hole was calculated for WZ structure $\mathrm{Mn}_{1-x}\mathrm{Zn}_x\mathrm{O}$ alloys at $x = 0$, 0.25, 0.5, 0.75, and 0.97, where the latter concentration corresponds to that of a $\mathrm{Mn}_{\mathrm{Zn}}$ impurity in a ZnO. In pure ZnO, we further considered an oxygen-localized $\mathrm{O}^{-\mathrm{I}}$ hole [34,42]. Table I lists the respective hole self-trapping energies E_{ST}. Exothermic energies (negative values) imply hole localization, leading to a small-polaron hopping mechanism; endothermic energies (positive values) imply that the delocalized bandlike state is energetically favorable, leading to the desirable band-conduction mechanism. In contrast to the case in the RS ground-state structure, the self-trapped hole is unstable in the WZ modification of MnO, where it is 0.23 eV higher in energy than the bandlike VBM state (Table I). As the Zn concentration increases, the energy difference is reduced, and the small-polaron state becomes favorable around $x \approx 0.7$, i.e., the point where the $\mathrm{Mn}^{+\mathrm{II}}/\mathrm{Mn}^{+\mathrm{III}}$ transition crosses the VBM energy. This composition dependence is also shown in Fig. 4, where the results from different sections of this article are illustrated in a combined graphic. The Zn-rich regime of the alloy can be described as Mn-doped ZnO, where an impurity band is formed because of the $\mathrm{Mn}_{\mathrm{Zn}}$ substitution. The $\mathrm{Mn}_{\mathrm{Zn}}$ impurity in ZnO acts as a hole-trapping defect with a hole-binding energy of −0.26 eV relative to the occupied Mn impurity band. In the extrapolation to the dilute $x \rightarrow 1$ limit, the $\mathrm{Mn}^{+\mathrm{II}}/\mathrm{Mn}^{+\mathrm{III}}$ transition corresponds to a deep donor level of $\mathrm{Mn}_{\mathrm{Zn}}$ at 0.71 eV above the VBM of ZnO (cf. Fig. 4). The formation of the $\mathrm{Mn}^{+\mathrm{III}}$ state due to hole self-trapping is associated with reduction of the Mn-O bond length by about 0.13 Å, irrespective of the composition x.

In pure ZnO, in the absence of Mn, the oxygen-localized self-trapped $\mathrm{O}^{-\mathrm{I}}$ hole was found to exist only as a metastable configuration 0.30 eV higher in energy than the delocalized VBM state (Table I), comparable to the case of the $\mathrm{Mn}^{+\mathrm{III}}$ hole in WZ MnO. Thus, ZnO is found to be a band conductor for hole transport. Summarizing the analysis of small-polaron formation and self-trapping, we expect

TABLE I. The calculated self-trapping E_{ST} energies for hole carriers in MnO, ZnO, and $\mathrm{Mn}_{1-x}\mathrm{Zn}_x\mathrm{O}$ alloys. In Mn-containing compounds, the small-polaron formation corresponds to the $\mathrm{Mn}^{+\mathrm{II}} + h^+ \rightarrow \mathrm{Mn}^{+\mathrm{III}}$ transition. In pure ZnO, the (unstable) hole polaron is localized at an oxygen anion, $\mathrm{O}^{-\mathrm{II}} + h^+ \rightarrow \mathrm{O}^{-I}$.

		E_{ST}(eV)
MnO (RS)		−0.33
MnO (WZ)		+0.23
$\mathrm{Mn}_{1-x}\mathrm{Zn}_x\mathrm{O}$	$x = 0.25$	+0.22
$\mathrm{Mn}_{1-x}\mathrm{Zn}_x\mathrm{O}$	$x = 0.50$	+0.07
$\mathrm{Mn}_{1-x}\mathrm{Zn}_x\mathrm{O}$	$x = 0.75$	+0.01
$\mathrm{Mn}_{\mathrm{Zn}}$ in ZnO	$x \rightarrow 1$	−0.26
ZnO (WZ)		+0.30

favorable bandlike transport for both electron and hole carriers in $Mn_{1-x}Zn_xO$ alloys around the composition $x = 0.5$, thereby avoiding an important bottleneck for opto-electronic applications. For example, the electron self-trapping in Fe_2O_3 [4,8,43] causes low electron mobilities and is a likely source for the rapid bulk recombination of electron-hole pairs [44].

Experimentally, we attempted *n*-type doping by Gallium, which is known as an efficient dopant in ZnO and in $Zn_{1-x}Mg_xO$ alloys [45]. From the calculated band-structure properties discussed above, we expect a shallow donor state with an ionization energy around 60 meV, close to that of ZnO and sufficiently small to generate free electrons at room temperature. For the combinatorial PLD growth of $Mn_{1-x-y}Zn_xGa_yO$ alloys, we used a ZnO target containing 4 cat.% Ga. Hence, the Ga doping level y_{Ga} varies with the Zn composition x in the compositional libraries, i.e., $y_{Ga} = 0.04 \cdot x$. Estimating the film thickness from XRF measurements [20], we determined the electrical conductivity by performing combinatorial, spatially resolved four-point probe measurements of the sheet resistance. For the same growth temperature of 297 °C as above, Fig. 3 shows the doping-specific conductivity, i.e., the conductivity in $S \cdot cm^{-1}$ normalized by the Ga content per formula unit (i.e., by y_{Ga}). The conductivity shows clear correlations with the alloy structure and composition (cf. Fig. 3): In the RS single-phase region ($x < 0.19$), there is no significant conductivity. A low level of 10 $S \cdot cm^{-1} \cdot y_{Ga}{}^{-1}$ is observed within the miscibility gap ($0.19 < x < 0.45$), where the microstructural features due to the coexistence of RS and WZ regions can be expected to impede the conduction.

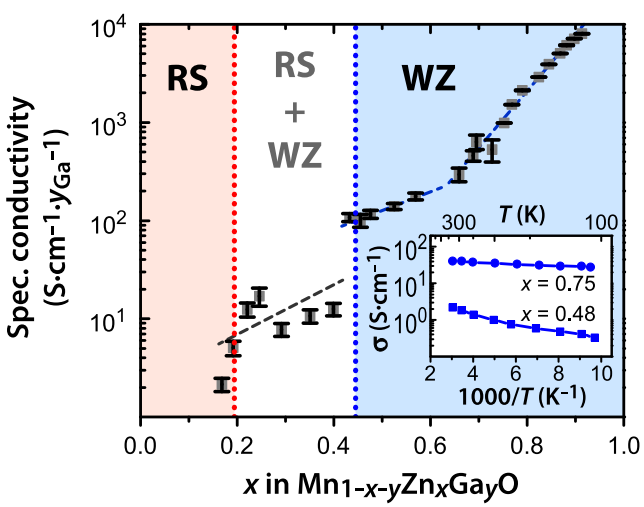

FIG. 3. Doping and electrical properties: The main graph shows the composition dependence of the experimentally measured doping-specific conductivity in Ga-doped $Mn_{1-x-y}Zn_xGa_yO$ grown at 297 °C. The dashed lines are guides to the eye to illustrate the different regimes of doping behavior. The inset shows the temperature dependence of the absolute conductivity for two single-composition samples.

An intermediate conductivity level of about 100 $S \cdot cm^{-1} \cdot y_{Ga}{}^{-1}$ is observed in the WZ single-phase region of $Mn_{1-x-y}Zn_xGa_yO$ alloys around $x = 0.5$. Approaching the pure ZnO composition, the doping-specific conductivity increases further up to 10^4 S cm^{-1} $y_{Ga}{}^{-1}$, corresponding to the high degenerate doping levels that are achievable in ZnO-based transparent conducting oxides [46]. Interestingly, the insulating behavior in the RS structure at lower Mn compositions suggests that the tetrahedral structure modification also affords a reduction of self-compensation [5], which is the likely cause for the absence of (electron) conductivity in the RS structure.

In order to determine the electron concentration and mobility, we performed Hall-effect measurements for two single-composition samples with $x = 0.48 (y_{Ga} = 0.02)$ and $x = 0.75 (y_{Ga} = 0.03)$, grown at the same temperature (297 °C) as above and under otherwise similar conditions as the combinatorial samples. At $x = 0.48$, we obtained, at room temperature, an absolute conductivity of 2 S /cm with an electron concentration of $n = 3 \times 10^{19}$ cm^{-3} and a mobility of $\mu = 0.4$ cm^2/Vs. Both carrier density and mobility increased with Zn composition, i.e., to $n = 1.0 \times 10^{20}$ cm^{-3} and $\mu = 3.5$ cm^2/Vs for $x = 0.75$. We further measured the temperature dependence of the conductivity, shown in the inset in Fig. 3. At $x = 0.48$, the conductivity exhibits a small activation energy of about 20 meV, and it is essentially temperature independent for the sample with $x = 0.75$. These observations support the expectation of shallow Ga dopants with degenerate doping levels in the higher doped sample. The positive correlation between n and μ suggests grain-barrier-limited transport [47], as often observed in ZnO thin-film samples [48,49]. In this case, the mobility measured on the thin-film sample is not an intrinsic materials property, and the actual intragrain (bulk) mobility can be much larger.

V. IONIZATION POTENTIAL AND ELECTRON AFFINITY

As a final step of the computational characterization, we determined the band lineup for the $Mn_{1-x}Zn_xO$ alloys with respect to the vacuum level by combining the GW band-structure calculations with DFT calculations of the potential step at the $11\bar{2}0$ surface, which is a typical low-energy nonpolar surface orientation in wurtzite semiconductors like ZnO [50,51]. Figure 4 shows the composition dependence of the conduction band minimum (CBM) and the VBM, corresponding to the electron affinity (EA) and the ionization potential (IP), respectively. We see in Fig. 4 that the IP of $Mn_{1-x}Zn_xO$ increases with the Zn composition, showing a discontinuity at $x = 1.0$ due to the above-mentioned impurity character of Mn_{Zn} in ZnO. (The development of an Mn impurity band in ZnO is schematically illustrated in Fig. 4. Please see Fig. 7 in Appendix A 2 for the composition dependence of the calculated density of

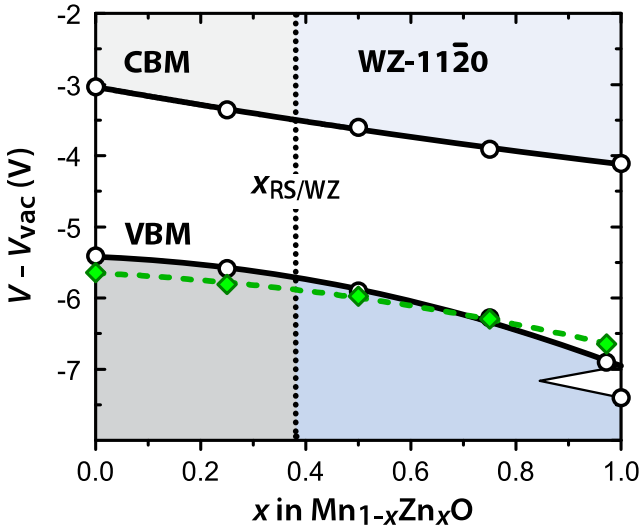

FIG. 4. Band lineup and hole-self-trapping level: The calculated CBM and the VBM energies relative to the vacuum potential (V_{vac}) at the 11$\bar{2}$0 surface of WZ structure $Mn_{1-x}Zn_xO$ alloys. Shown are the calculated EA and IP data points (circles) and a fit (solid lines) up to quadratic order [cf. Eq. (2)], where the emergence of an Mn impurity band close to the ZnO composition is indicated schematically. The calculated polaronic Mn^{+II}/Mn^{+III} transition level (diamonds and dashed line) lies below the VBM for $x < 0.7$, indicating that band conduction prevails over a small-polaron transport mechanism at these compositions.

states.) Taking into account the quasiparticle energy of the occupied Mn_{Zn} state at 0.45 eV above the VBM of ZnO, determined from the GW defect calculation, and the self-trapping energy from the polaron theory, we find that the Mn_{Zn} defect causes an optical absorption band at 2.84 eV with a zero-phonon transition at 2.58 eV, which is consistent with absorption and photoconductivity measurements in Mn-doped ZnO [28].

For potential application as a photo-anode material, the alignment of the valence band relative to the H_2O/O_2 redox potential is of great importance. Similar to TiO_2, ZnO also has an undesirably large offset between the VBM and the redox potential [52,53]. Taking the vacuum potential as a suitable reference for the band lineup [15], we see in Fig. 4 that the VBM of $Mn_{1-x}Zn_xO$ lies about 1.5 eV above that of ZnO at compositions around $x \approx 0.5$. This finding suggests that the $Mn_{1-x}Zn_xO$ alloys have the potential for optimizing the tradeoff between the magnitude of the band gap and the alignment of the band edges with the redox potentials. A recent theoretical study [12] also arrived at this conclusion, albeit for the octahedral rocksalt structure of $Mn_{1-x}Zn_xO$, which was shown here to be unstable in the composition range of interest and which would not benefit from the improved optical, transport, and doping properties present in the tetrahedral wurtzite structure.

VI. PHOTO-ELECTROCATALYTIC MEASUREMENTS

As an initial test of the viability of the tetrahedral $Mn_{1-x}Zn_xO$ alloys for photo-electrocatalysis and to obtain an experimental validation of the predicted advantageous hole-transport mechanism, we performed photo-electrochemical measurements and report here initial results [18]. To this end, we grew $Mn_{0.5}Zn_{0.5}O$ samples with different thicknesses on conductive fluorine-doped SnO_2 (FTO) glass substrates, which serve as a back contact. Figure 5(a) shows the current density j of a 673-nm-thick MnZnO sample as a function of the applied potential relative to an Ag/AgCl electrode in a K_2SO_4 solution (see also Appendix A 8). The photoresponse Δj was determined by modulated illumination (light chopper), for both front (MnZnO-facing) and back (FTO/glass-facing) illumination. All films exhibited an anodic photocurrent, implying the transport of hole carriers across the semiconductor or electrolyte interface.

Figure 5(b) shows the photoresponse at the potential of 1.4 V as a function of the thickness d of the MnZnO

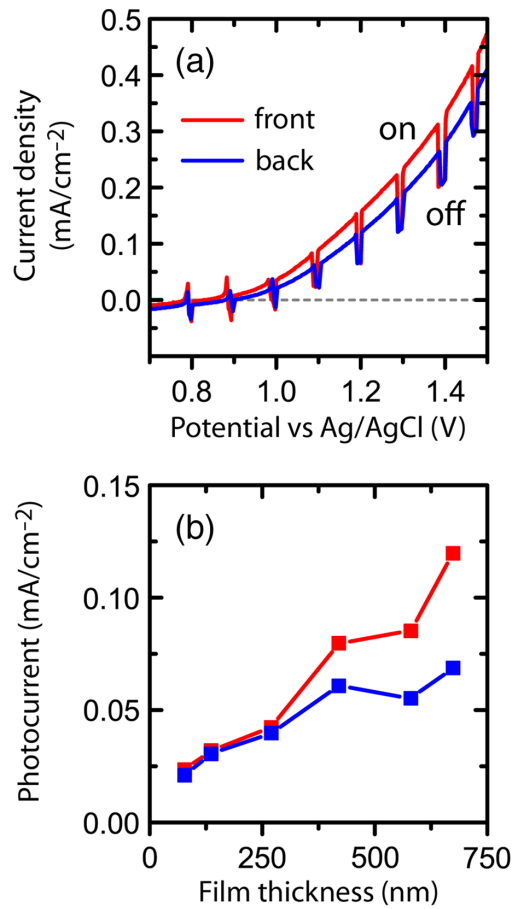

FIG. 5. (a) Current density for a 673-nm-thick $Mn_{0.5}Zn_{0.5}O$ sample under modulated illumination (on/off), for both front and back illumination, as a function of the applied voltage. (b) The photocurrent (on/off difference), measured at 1.4 V, as a function of the film thickness.

film. For front illumination, the photocurrent increases from $\Delta j_f = 21.5\ \mu A/cm^2$ for $d = 76$ nm to $\Delta j_f = 119.7\ \mu A/cm^2$ for $d = 673$ nm. The continuous increase of Δj_f with d suggests that photogenerated hole carriers throughout the entire film contribute to the photocurrent. Switching the illumination direction provides additional information about the carrier type limiting the charge collection [54]. In the case of back illumination, the photocurrent Δj_b essentially equals that of front illumination for film thicknesses below 300 nm [see Fig. 5(b)], but it starts to fall short of Δj_f for thicker films. These observations strongly suggest that hole transport is not a rate-limiting factor up to thicknesses of at least 300 nm. Such large hole collection lengths are not plausible for a small-polaron conduction mechanism for holes. (Depending on the magnitude of the energy barrier for hole hopping, the diffusion length may be only in the order of a lattice constant for a small-polaron transport mechanism.) Thus, the present photo-electrocatalytic experiments strongly support the favorable hole transport mechanism in MnZnO alloys predicted by the theory above in Sec. IV. Given that the photocurrent Δj_f continues to increase with film thickness beyond the absorption length (<300 nm), the recombination of holes at the FTO back contact is likely the rate-limiting step for the present devices. Device optimization should lead to significant further increases of the photoresponse.

VII. CONCLUSIONS

In the present work, we have used computation and combinatorial synthesis and characterization to design a novel transition metal oxide material, i.e., $Mn_{1-x}Zn_xO$ alloys with favorable semiconducting properties in the composition range around $x \approx 0.5$, including the band gap, optical absorption, the transport mechanism for carriers, dopability, and the band lineup relative to the vacuum level for potential solar water-splitting application. These properties were enabled by the deliberate manipulation of the coordination symmetry of MnO, i.e., the transition from the rocksalt to the wurtzite structure by alloying with ZnO. The alloy compositions of interest lie deep inside the miscibility gap, but the thermodynamic solubility limit was overcome by nonequilibrium growth with PLD. Initial photo-electrocatalytic measurements on devices based on these novel alloys provide a proof of principle and, in particular, corroborate the predicted band transport mechanism for hole carriers.

ACKNOWLEDGMENTS

This work was supported by the U.S. Department of Energy, Office of Science, Office of Basic Energy Sciences, as part of an Energy Frontier Research Center under Contract No. DE-AC36-08GO28308 to NREL. This work used computational resources sponsored by the Department of Energy's Office of Energy Efficiency and Renewable Energy, located at NREL.

APPENDIX: COMPUTATIONAL AND EXPERIMENTAL DETAILS

1. Electronic structure methods

The DFT and GW calculations in this study were performed using the projector-augmented wave (PAW) implementation in the Vienna *ab initio* simulation package (VASP) [26,55], using the Perdew-Burke-Ernzerhof (PBE) generalized gradient approximation (GGA) for the exchange-correlation functional [56]. The GGA + U method [57] with $U = 3$ eV was employed for Mn-d orbitals in all DFT calculations. For the Zn-d orbitals, standard GGA describes the structural features (e.g., lattice constants) more consistently than GGA + U. However, a $U = 6$ eV was applied to Zn-d orbitals in those cases where a correct description of the p-d hybridization is important, i.e., for the calculation of the wave functions for subsequent GW [27] or RPA [11] calculations, as well as for the calculation of small-polaron binding energies [34]. GGA + U for Zn-d was also used in order to maintain the compatibility between the GW and the DFT surface calculations (see below). In the GW calculations, the GGA + U wave functions were kept, but the eigenenergies were iterated to self-consistency. The detailed computational settings used for the GW band-gap calculations are identical to those published before [8,27], including the use of an onsite potential to account for the underbinding of Zn-d states in GW [27]. The present GW approach has been shown before to provide accurate band structures for the normal rocksalt phase of MnO [8] and for wurtzite ZnO [27].

Standard DFT, DFT + U, and even hybrid functional approaches have been found to describe the polymorphic energy ordering of MnO with insufficient accuracy [58]. In order to overcome these issues, we performed previous total-energy calculations in the random phase approximation (RPA) [11]. Please see Ref. [11] for the detailed results for the RPA energies of MnO in the RS and ZB structures, and of ZnO in the RS, ZB, and WZ structures. Because of the magnetic configuration, the smallest unit cell for WZ-MnO contains 16 atoms, which proved unfeasible for computing intensive RPA calculations. Since the energies of the ZB and WZ structures are degenerate within about 10 meV in DFT-based functionals (GGA + U, hybrid functionals), we use here the ZB energy as an approximation to the WZ energy.

The optical absorption spectra were determined from the dielectric function, calculated both in the independent particle approximation, using the PAW implementation of Ref. [59], and including electron-hole interactions (excitonic effects) via time-dependent density functional theory (TD-DFT). In the TD-DFT calculations, we used a hybrid functional kernel [29] with a fraction of Fock exchange of $\alpha = 1/\varepsilon$, where ε is the static electronic

dielectric constant obtained from the preceding GW calculation. The **k** derivatives of the electron orbitals were determined using the finite difference approximation of Ref. [60] in the "perturbation expansion after discretization" formulation. For the calculation of optical properties, the k-point density was increased to $7000/n_{\mathrm{at}}$ within the full Brillouin zone, where n_{at} is the number of atoms in the unit cell. In order to keep these calculations feasible, we reduced the energy cutoff for the response functions and reduced the number of bands to $32 \times n_{\mathrm{at}}$, as compared to $64 \times n_{\mathrm{at}}$ for the band-gap calculations using a coarser grid with about $1000/n_{\mathrm{at}}$k points. The resulting band-gap changes of less than 0.1 eV were corrected for in the spectra shown in Fig. 2(a). The absorption spectrum is subject to a finite Lorentzian broadening in these calculations, and despite the increased k-point density, the subgap absorption due to the bound exciton was not accurately resolved. The low-energy part of the spectrum, where the absorption coefficient is significantly affected by the broadening, is omitted [Fig. 2(a)]. From the calculated effective masses, and dielectric constants ($\varepsilon = 8.1$ and 7.8 for WZ-MnO and ZnO, respectively, including the ionic contribution), we expect a Wannier-type exciton with a binding energy similar to that in ZnO, i.e., about 60 meV. The electron effective masses were obtained directly from the band energies close to the conduction band minimum (CBM) at the Γ point of the Brillouin zone. Because of a larger nonparabolicity and anisotropy in the valence band, for hole carriers, we determined instead the density-of-states effective masses (cf. Ref. [61]) by integrating the density of states weighted with a Boltzmann distribution at 1000 K.

2. Models for alloys and the magnetic structure

In order to model the alloy systems, we used special quasirandom structures (SQS) [62]. The SQS in this work were generated with the *mcsqs* utility in the Alloy Theoretic Automated Toolkit (ATAT) [63]. To calculate the mixing energy, we employed SQS with 64 atoms, without any constraints other than the composition being $x = 0/16, 1/16, \ldots 16/16$, while keeping the underlying magnetic sublattices of the low-energy antiferromagnetic configuration "AF1" of wurtzite structure MnO [57]. A structural model of the atomic configuration for $x = 0.5$ is shown in Fig. 6 (created with the VMD software [64]), showing also the calculated lattice parameters for the end compounds WZ MnO and ZnO. For the polaron calculations, we used 64-atom SQS supercells with the shape close to a cube, as well as a 72-atom ZnO supercell for the $\mathrm{Mn_{Zn}}$ impurity. At room temperature, MnO is paramagnetic (PM). It is important, however, to consider that in the PM phase the moments are not completely random, but the local (short-range) antiferromagnetic (AFM) order persists far above the Neel temperature [65], even in the absence of long-range AFM order. More recently, Hughes and co-workers calculated the electronic structure for rocksalt MnO in the PM phase with the "disordered local moment" method [66]. Their results show that the insulating gap in the PM state is practically identical to that in the AFM phase. Thus, we conclude that our assumption of an AFM order is an appropriate model of the magnetic structure for computing the electronic structure in this system. For the GW calculations, we generated smaller 32-atom SQS for the alloy compositions $x = 0.25$, 0.5, and 0.75, constructed to maintain the symmetry between the spin-up and spin-down density of states.

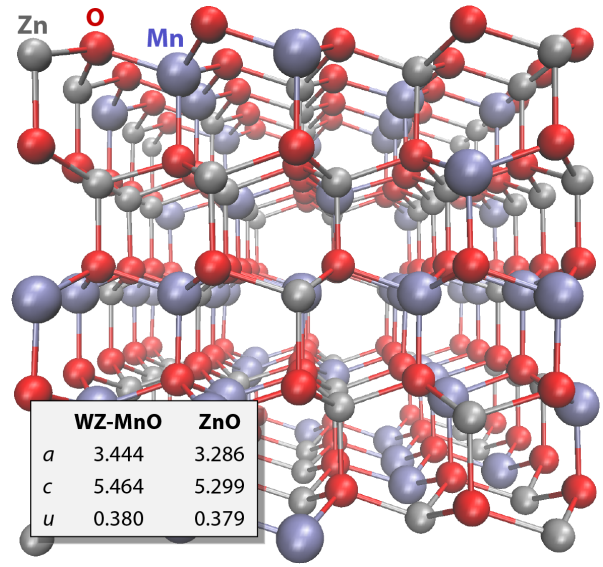

FIG. 6. Structural model of the SQS used to represent the $\mathrm{Mn_{0.5}Zn_{0.5}O}$ alloy. The inserted table shows the similarity of the calculated lattice parameters for WZ MnO and ZnO.

Figure 7 shows the calculated local density of states (LDOS) for the valence band of the $\mathrm{Mn_{1-x}Zn_xO}$ alloys, as obtained from the GW quasiparticle energy calculations, where the contributions from all sites of the same atom type (Mn, Zn, or O) have been averaged. The energy scale is aligned with respect to the vacuum level, as in Fig. 4. We see that at high Zn compositions, Mn forms an impurity band in ZnO, but at $x = 0.75$ and lower Zn compositions, the alloys exhibit a continuous valence band with dominating contributions from Mn-d and O-p.

3. Calculation of the small-polaron self-trapping energies

The hole self-trapping energies are calculated using the *ab initio* theory for the small-polaron binding energies of Refs. [34,35]. This approach employs a potential term V_{hs}, i.e., the "hole-state potential," which is added to the DFT Hamiltonian. A potential strength parameter λ_{hs} is then adjusted to recover the quasiparticle energy condition ("Koopmans condition") and linearity of the total energy $E(N)$, thereby overcoming the well-known delocalization error of standard DFT functionals [41] and enabling a

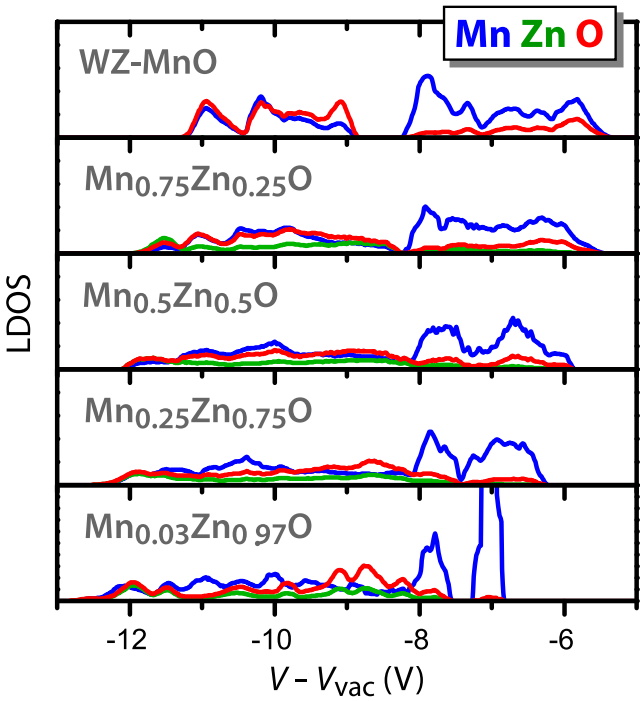

FIG. 7. Averaged local density of states (LDOS) of Mn, Zn, and O sites in $Mn_{1-x}Zn_xO$ alloys, showing the development of an Mn impurity band at high Zn compositions.

quantitative prediction of small-polaron binding energies. For the pure binary MnO, in Ref. [8] we used a hole-state potential $V_{hs} = \lambda_{hs}(1 - n_{m,\sigma}/n_{ref})$ constructed in analogy to the original case of O-p holes [34] such that the additional potential vanishes for the occupied Mn-d^5 manifold in the local majority spin channel ("spin-up"), as long as there is no self-trapped hole carrier. In contrast to the O-p^6 case of Ref. [34], however, V_{hs} indirectly affects the charge density by acting on the unoccupied minority spin channel ("spin-down"). While in pure MnO, this indirect effect has no obvious consequences other than increasing the exchange splitting, we found that in the ZnO:Mn impurity limit, it leads to a hybridization of the Mn state with the valence band of ZnO that is inconsistent with the result of the GW defect calculation, and it prohibits the correct prediction of the carrier localization in the Mn^{+III} state. In order to reconcile the ZnO:Mn case, we therefore defined a spin-dependent hole-state potential $V_{hs,\sigma}$ that acts only on the spin-up channel, thereby recovering the original idea that the hole-state potential should not affect the charge density (in either spin channel) in the absence of a localized hole carrier [34]. The composition dependence of the self-trapping energy E_{ST}, which equals the energy difference between the Mn^{+II}/Mn^{+III} transition and the valence band maximum (VBM), is given in Table I and shown also in Fig. 4. In the case of the alloy systems, the sampling over Mn ions at five different lattice sites resulted in a standard deviation of 0.06 eV. For pure ZnO, we used $\lambda_{hs} = 4.5$ eV for the O-p orbitals, as determined before in Ref. [67] for the case of GGA + U ($U = 6$ eV for Zn-d) as the underlying DFT functional. In order to determine the structural configuration of the distorted ZnO lattice in the presence of a (metastable) self-trapped hole, we used an initial configuration similar to that of the charge-neutral Li_{Zn} defect and then relaxed the structure to the nearest local minimum.

4. Surface calculations

In order to align the VBM and CBM energies relative to the vacuum level (Fig. 4), we constructed slab supercells for the $11\bar{2}0$ surface of the WZ lattice, containing 80 atoms for ZnO and 160 atoms for MnO (to accommodate the magnetic structure of wurtzite MnO). These slab calculations in the GGA + U approximation yield the potential step between the average potential in the semiconductor and the vacuum. The potential step for alloys was determined by linear interpolation between $MnO(x = 0)$ and $ZnO(x = 1)$. Since the GW quasiparticle energies are defined directly with respect to the average potential, the GW predictions for the ionization potential and the electron affinity are obtained by simple addition of the potential step and the quasiparticle energy of the VBM and the CBM, respectively.

5. Combinatorial synthesis

$Mn_{1-x}Zn_xO$ alloy thin films were grown on $2'' \times 2''$ glass substrates by pulsed laser deposition using a KrF excimer laser (Spectra-Physics) operating at 248 nm with a pulse duration of 25 ns. We employed a thin-film high-throughput combinatorial approach [20,21] to deposit "libraries" with a spatial gradient in both the composition [22] and the substrate temperature [23], using commercial 2-inch targets (purity 99.99%) of MnO, ZnO, and 4% Ga-doped ZnO. A calibration process was performed to express the substrate temperature as a function of the position on the substrate and the set-point temperature [23]. The laser was operated at 40 Hz, and the beam was focused through a 60-cm lens onto the rotating targets at a 45° angle, with a laser fluence of 4 J/cm^2 on the target surface. The target-substrate distance was fixed to 7 cm. The growth chamber was evacuated to the base pressure of 10^{-9} Torr and backfilled with an Ar/O_2 mixture to a working pressure of 5×10^{-3} Torr with an O_2/Ar ratio of 1/100. The thickness of the films grown for this work varied between 130 and 160 nm.

6. Combinatorial characterization

The properties of the combinatorial samples were automatically mapped at 44 points, corresponding to a grid of 4 substrate temperatures and 11 compositions. X-ray fluorescence spectra were collected with a 300s scan time using a Matrix Metrologies MaXXi 5 with a W anode and a 800-μm collimator. The resulting spectra were modeled

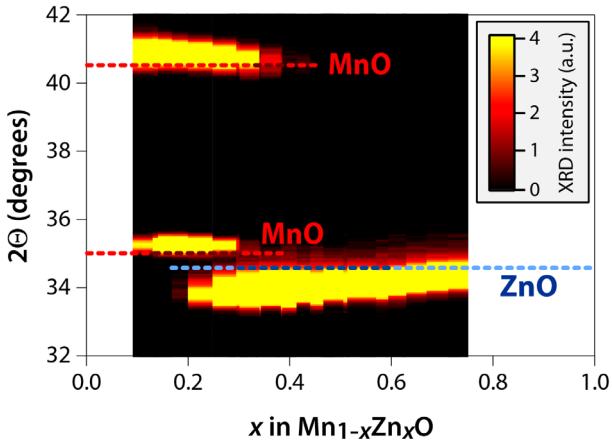

FIG. 8. Contour plot of the composition dependence of the XRD pattern for the $Mn_{1-x}Zn_xO$ library deposited at 297 °C. The dashed lines show the reference data for the (111) and (200) reflections of RS-MnO at $2\Theta = 35.0°$ and 40.6°, respectively, and for the (002) reflection of WZ-ZnO at 34.6°.

using the MTF-FP software to obtain both the chemical composition and the thickness of the samples. The accuracy of the thickness measurement was verified by spectroscopic ellipsometry (J. A. Woollam M-2000S). The x-ray diffraction (XRD) patterns of Cu $K\alpha$ radiation were collected using a Bruker D8 Discover. The RS and WZ diffraction peaks were assigned based on the reference data for MnO and ZnO from the Inorganic Crystal Structure Database (ICSD) and from reference samples of the binary oxides grown under similar conditions. The combinatorial XRD mapping of the sample grown at 297 °C is shown in Fig. 8. The RS/WZ phase-boundary compositions were obtained by the "disappearing phase method" [24], and the data points and error bars (standard deviation) shown in Fig. 1(b) were determined by sampling of the results from six compositional libraries. The optical spectra were mapped in the 300–2000-nm range using a fiber-optics-based spectrometer with normally incident angle of light generated by deuterium and tungsten-halogen light sources and collected using Si and InGaAs detector arrays. The measured transmittance (T) and reflectance (R) spectra were converted into the absorption coefficient α using the relationship $\alpha = -\ln[T/(1-R)]/d$, where d is the film thickness. The Tauc plot for the measured absorption spectrum (cf. Fig. 2) for the composition $x = 0.5$ is shown in Fig. 9. Fitting the linear portion of $(\alpha E)^2$ yields a band gap of 2.29 eV. The measurements of the electrical conductivity were carried out using a four-point probe mapping method.

7. Single-composition samples for Hall measurements

Ga-doped single-composition samples ($x = 0.48$ and $x = 0.75$) with a thickness of 130 nm were grown from the same targets as above, using rotating $1'' \times 1''$ substrates.

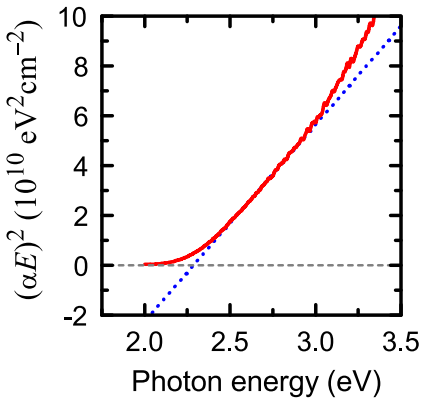

FIG. 9. The Tauc analysis of the experimentally measured absorption spectrum for $Mn_{0.5}Zn_{0.5}O$ (cf. Fig. 2).

The compositional homogeneity was confirmed by XRF measurements. Using temperature calibration of the single-composition setup, the temperature was adjusted to 297 °C, i.e., the same growth temperature as for the results shown in Figs. 2(b), 3 and 8 for combinatorial samples. Otherwise, the PLD parameters are identical to those described above. The single-composition samples were characterized using an Accent HL5500PC Hall-effect measurement system.

8. Photo-electrocatalytic characterization

The devices for photo-electrocatalytic characterization were fabricated by deposition of single-composition ($x = 0.51$) $Mn_{1-x}Zn_xO$ samples on FTO glass substrates at a growth temperature of 397 °C. The electrochemical measurements were performed using a CH Instruments 660 A electrochemical analyzer with a conventional three electrodes system that consists of a platinum foil as a counter electrode, an Ag/AgCl (with saturated KCl) reference electrode, and the MnZnO/FTO working electrode. The electrolyte was a 0.5 mol/L K_2SO_4 solution with a pH 10. A 250-W tungsten lamp solar simulator from Newport Instruments was used as a light source (calibrated to global AM1.5 intensity with a reference cell). The samples were illuminated from both the front and back sides of the MnZnO photoelectrodes using a light chopper. An insulating epoxy was used to cover the margins of the MnZnO/FTO/glass structure.

[1] J. C. Phillips, *Bonds and Bands in Semiconductors* (Academic Press, New York, 1973).
[2] G. R. Fleming and M. A. Ratner, *Grand Challenges in Basic Energy Sciences*, Phys. Today **61**, 28 (2008).
[3] D. C. Look, *Recent Advances in ZnO Materials and Devices*, Mater. Sci. Eng. B **80**, 383 (2001).
[4] A. J. Bosman and H. J. van Daal, *Small-Polaron Versus Band Conduction in Some Transition-Metal Oxides*, Adv. Phys. **19**, 1 (1970).

[5] G. Mandel, *Self-Compensation Limited Conductivity in Binary Semiconductors. I. Theory*, Phys. Rev. **134**, A1073 (1964).

[6] O. Khaselev and J. A. Turner, *A Monolithic Photovoltaic-Photoelectrochemical Device for Hydrogen Production via Water Splitting*, Science **280**, 425 (1998).

[7] K. Sivula, F. Le Formal, and M. Grätzel, *Solar Water Splitting: Progress Using Hematite (α-Fe_2O_3) Photoelectrodes*, Chem. Sus. Chem. **4**, 432 (2011).

[8] H. Peng and S. Lany, *Semiconducting Transition-Metal Oxides Based on d^5 Cations: Theory for MnO and* Fe_2O_3, Phys. Rev. B **85**, 201202(R) (2012).

[9] K. M. Nam, Y.-I. Kim, Y. Jo, S. M. Lee, B. G. Kim, R. Choi, S.-I. Choi, H. Song, and J. T. Park, *New Crystal Structure: Synthesis and Characterization of Hexagonal Wurtzite MnO*, J. Am. Chem. Soc. **134**, 8392 (2012).

[10] R. Seshadri, *Zinc Oxide-Based Diluted Magnetic Semiconductors*, Curr. Opin. Solid State Mater. Sci. **9**, 1 (2005).

[11] H. Peng and S. Lany, *Polymorphic Energy Ordering of MgO, ZnO, GaN, and MnO within the Random Phase Approximation*, Phys. Rev. B **87**, 174113 (2013).

[12] D. K. Kanan and E. A. Carter, *Band Gap Engineering of MnO via ZnO Alloying: A Potential New Visible-Light Photocatalyst*, J. Phys. Chem. C **116**, 9876 (2012).

[13] D. K. Kanan and E. A. Carter, *Ab Initio Study of Electron and Hole Transport in Pure and Doped MnO and MnO: ZnO Alloy*, J. Mater. Chem. A **1**, 9246 (2013).

[14] C. H. Bates, W. B. White, and R. Roy, *The Solubility of Transition Metal Oxides in Zinc Oxide and the Reflectance Spectra of* Mn^{2+} *and* Fe^{2+} *in Tetrahedral Fields*, J. Inorg. Nucl. Chem. **28**, 397 (1966).

[15] V. Stevanovic, S. Lany, D. S. Ginley, W. Tumas, and A. Zunger, *Assessing Capability of Semiconductors to Split Water Using Ionization Potentials and Electron Affinities Only*, Phys. Chem. Chem. Phys. **16**, 3706 (2014).

[16] A. K. Sharma, J. Narayan, J. F. Muth, C. W. Teng, C. Jin, A. Kvit, R. M. Kolbas, and O. W. Holland, *Optical and Structural Properties of Epitaxial* $Mg_xZn_{1-x}O$ *Alloys*, Appl. Phys. Lett. **75**, 3327 (1999).

[17] A. Zakutayev, N. H. Perry, T. O. Mason, D. S. Ginley, and S. Lany, *Non-Equilibrium Origin of High Electrical Conductivity in Gallium Zinc Oxide Thin Films*, Appl. Phys. Lett. **103**, 232106 (2013).

[18] P. F. Ndione, E. L. Ratcliff, S. R. Dey, E. L. Warren, H. Peng, S. Lany, T. G. Deutsch, A. Zakutayev, and D. S. Ginley, *Rapid Screening of MnO-ZnO, a New Oxide-Alloy System for Water Splitting Applications* (unpublished).

[19] A. van de Walle and G. Ceder, *The Effect of Lattice Vibrations on Substitutional Alloy Thermodynamics*, Rev. Mod. Phys. **74**, 11 (2002).

[20] A. Zakutayev, F. J. Luciano, V. P. Bollinger, A. K. Sigdel, P. F. Ndione, J. D. Perkins, J. J. Berry, P. A. Parilla, and D. S. Ginley, *Development and Application of an Instrument for Spatially Resolved Seebeck Coefficient Measurements*, Rev. Sci. Instrum. **84**, 053905 (2013).

[21] A. Zakutayev, T. R. Paudel, P. F. Ndione, J. D. Perkins, S. Lany, A. Zunger, and D. S. Ginley, *Cation Off-Stoichiometry Leads to High p-Type Conductivity and Enhanced Transparency in* Co_2ZnO_4 *and* Co_2NiO_4 *Thin Films*, Phys. Rev. B **85**, 085204 (2012).

[22] A. Zakutayev, J. D. Perkins, P. A. Parilla, N. E. Widjonarko, A. K. Sigdel, J. J. Berry, and D. S. Ginley, *Zn–Ni–Co–O Wide-Band-Gap p-Type Conductive Oxides with High Work Functions*, MRS Commun.**1**, 23 (2011).

[23] A. Subramaniyan, J. D. Perkins, R. P. O'Hayre, S. Lany, V. Stevanovic, D. S. Ginley, and A. Zakutayev, *Non-Equilibrium Deposition of Phase Pure* Cu_2O *Thin Films at Reduced Growth Temperature*, APL Mater. **2**, 022105 (2014).

[24] B. D. Cullity, *Elements of X-Ray Diffraction* (Addison-Wesley, Reading, MA, 1959).

[25] L. Hedin, *New Method for Calculating the One-Particle Green's Function with Application to the Electron-Gas Problem*, Phys. Rev. **139**, A796 (1965).

[26] M. Shishkin and G. Kresse, *Implementation and Performance of the Frequency-Dependent GW Method within the PAW Framework*, Phys. Rev. B **74**, 035101 (2006).

[27] L. Y. Lim, S. Lany, Y. J. Chang, E. Rotenberg, A. Zunger, and M. F. Toney, *Angle-Resolved Photoemission and Quasiparticle Calculation of ZnO: The Need for d Band Shift in Oxide Semiconductors*, Phys. Rev. B **86**, 235113 (2012).

[28] C. A. Johnson, K. R. Kittilstved, T. C. Kaspar, T. C. Droubay, S. A. Chambers, G. M. Salley, and D. R. Gamelin, *Mid-Gap Electronic States in* $Zn_{1-x}Mn_xO$, Phys. Rev. B **82**, 115202 (2010).

[29] J. Paier, M. Marsman, and G. Kresse, *Dielectric Properties and Excitons for Extended Systems from Hybrid Functionals*, Phys. Rev. B **78**, 121201(R) (2008).

[30] Y. Tanabe and S. Sugano, *On the Absorption Spectra of Complex Ions II*, J. Phys. Soc. Jpn. **9**, 766 (1954).

[31] G. Hautier, A. Miglio, D. Waroquiers, G.-M. Rignanese, and X. Gonze, *How Does Chemistry Influence Electron Effective Mass in Oxides? A High-Throughput Computational Analysis*, Chem. Mater. **26**, 5447 (2014).

[32] H. Fröhlich, *Electrons in Lattice Fields*, Adv. Phys. **3**, 325 (1954).

[33] T. Holstein, *Studies of Polaron Motion: Part II. The "Small" Polaron*, Ann. Phys. (N.Y.) **8**, 343 (1959).

[34] S. Lany and A. Zunger, *Polaronic Hole Localization and Multiple Hole Binding of Acceptors in Oxide Wide-Gap Semiconductors*, Phys. Rev. B **80**, 085202 (2009).

[35] S. Lany, *Predicting Polaronic Defect States by Means of Generalized Koopmans Density Functional Calculations*, Phys. Status Solidi (b) **248**, 1052 (2011).

[36] C. Rödl, F. Fuchs, J. Furthmüller, and F. Bechstedt, *Quasiparticle Band Structures of the Antiferromagnetic Transition-Metal Oxides MnO, FeO, CoO, and NiO*, Phys. Rev. B **79**, 235114 (2009).

[37] H. Peng, A. Zakutayev, S. Lany, T. R. Paudel, M. d'Avezac, P. F. Ndione, J. D. Perkins, D. S. Ginley, A. R. Nagaraja, N. H. Perry, T. O. Mason, and A. Zunger, *Li-Doped* Cr_2MnO_4*: A New p-Type Transparent Conducting Oxide by Computational Materials Design*, Adv. Funct. Mater. **23**, 5267 (2013).

[38] A. R. Nagaraja, K. H. Stone, M. F. Toney, H. Peng, S. Lany, and T. O. Mason, *Experimental Characterization of a Theoretically-Designed Candidate p-Type Transparent Conducting Oxide: Li-Doped* Cr_2MnO_4, Chem. Mater. **26**, 4598 (2014).

[39] S. Lany and A. Zunger, *Polaronic Hole Localization and Multiple Hole Binding of Acceptors in Oxide Wide-Gap Semiconductors*, Phys. Rev. B **80**, 085202 (2009).

[40] S. Lany, *Predicting Polaronic Defect States by Means of Generalized Koopmans Density Functional Calculations*, Phys. Status Solidi (b) **248**, 1052 (2011).

[41] P. Mori-Sanchez, A. J. Cohen, and W. Yang, *Localization and Delocalization Errors in Density Functional Theory and Implications for Band-Gap Prediction*, Phys. Rev. Lett. **100**, 146401 (2008).

[42] O. F. Schirmer, *Holes Bound as Small Polarons to Acceptor Defects in Oxide Materials: Why Are Their Thermal Ionization Energies So High?*, J. Phys. Condens. Matter **23**, 334218 (2011).

[43] K. M. Rosso, D. M. A. Smith, and M. Dupuis, *An Ab Initio Model of Electron Transport in Hematite (α-Fe_2O_3) Basal Planes*, J. Chem. Phys. **118**, 6455 (2003).

[44] S. R. Pendlebury, M. Barroso, A. J. Cowan, K. Sivula, J. Tang, M. Grätzel, D. Klug, and J. R. Durrant, *Dynamics of photogenerated holes in nanocrystalline α-Fe_2O_3 electrodes for water oxidation probed by transient absorption spectroscopy*, Chem. Commun. (Cambridge) **47**, 716 (2011).

[45] Y. Ke, S. Lany, J. J. Berry, J. D. Perkins, P. A. Parilla, A. Zakutayev, T. Ohno, R. P. O'Hayre, and D. S. Ginley, *Enhanced Electron Mobility Due to Dopant-Defect Pairing in Conductive ZnMgO*, Adv. Funct. Mater. **24**, 2875 (2014).

[46] V. Bhosle, A. Tiwari, and J. Narayan, *Metallic Conductivity and Metal-Semiconductor Transition in Ga-Doped ZnO*, Appl. Phys. Lett. **88**, 032106 (2006).

[47] J. Y. W. Seto, *The Electrical Properties of Polycrystalline Silicon Films*, J. Appl. Phys. **46**, 5247 (1975).

[48] K. Ellmer and G. Vollweiler, *Electrical Transport Parameters of Heavily-Doped Zinc Oxide and Zinc Magnesium Oxide Single and Multilayer Films Heteroepitaxially Grown on Oxide Single Crystals*, Thin Solid Films **496**, 104 (2006).

[49] S. Cornelius, M. Vinnichenko, N. Shevchenko, A. Rogozin, A. Kolitsch, and W. Möller, *Achieving High Free Electron Mobility in ZnO:Al Thin Films Grown by Reactive Pulsed Magnetron Sputtering*, Appl. Phys. Lett. **94**, 042103 (2009).

[50] O. Dulub, L. A. Boatner, and U. Diebold, *STM Study of the Geometric and Electronic Structure of ZnO(0001)-Zn, (000-1)-O, (10-10), and (11-20) Surfaces*, Surf. Sci. **519**, 201 (2002).

[51] B. Meyer and D. Marx, *Density-Functional Study of the Structure and Stability of ZnO Surfaces*, Phys. Rev. B **67**, 035403 (2003).

[52] A. J. Nozik and R. Memming, *Physical Chemistry of Semiconductor—Liquid Interfaces*, J. Phys. Chem. **100**, 13061 (1996).

[53] M. Grätzel, *Photoelectrochemical Cells*, Nature (London) **414**, 338 (2001).

[54] Y. Liang, T. Tsubota, L. P. A. Mooij, and R. van de Krol, *Highly Improved Quantum Efficiencies for Thin Film $BiVO_4$ Photoanodes*, J. Phys. Chem. C **115**, 17594 (2011).

[55] G. Kresse and D. Joubert, *From Ultrasoft Pseudopotentials to the Projector Augmented-Wave Method*, Phys. Rev. B **59**, 1758 (1999).

[56] J. P. Perdew, K. Burke, and M. Ernzerhof, *Generalized Gradient Approximation Made Simple*, Phys. Rev. Lett. **77**, 3865 (1996).

[57] S. L. Dudarev, G. A. Botton, S. Y. Savrasov, C. J. Humphreys, and A. P. Sutton, *Electron-Energy-Loss Spectra and the Structural Stability of Nickel Oxide: An* LSDA + U *Study*, Phys. Rev. B **57**, 1505 (1998).

[58] A. Schrön, C. Rödl, and F. Bechstedt, *Energetic Stability and Magnetic Properties of MnO in the Rocksalt, Wurtzite, and Zinc-Blende Structures: Influence of Exchange and Correlation*, Phys. Rev. B **82**, 165109 (2010).

[59] M. Gajdoš, K. Hummer, G. Kresse, J. Furthmüller, and F. Bechstedt, *Linear Optical Properties in the Projector-Augmented Wave Methodology*, Phys. Rev. B **73**, 045112 (2006).

[60] R. W. Nunes and X. Gonze, *Berry-Phase Treatment of the Homogeneous Electric Field Perturbation in Insulators*, Phys. Rev. B **63**, 155107 (2001).

[61] G. Trimarchi, H. Peng, J. Im, A. J. Freeman, V. Cloet, A. Raw, K. R. Poeppelmeier, K. Biswas, S. Lany, and A. Zunger, *Using Design Principles to Systematically Plan the Synthesis of Hole-Conducting Transparent Oxides: Cu_3VO_4 and Ag_3VO_4 as a Case Study*, Phys. Rev. B **84**, 165116 (2011).

[62] S. H. Wei, L. G. Ferreira, J. E. Bernard, and A. Zunger, *Electronic Properties of Random Alloys: Special Quasirandom Structures*, Phys. Rev. B **42**, 9622 (1990).

[63] A. van de Walle, *Multicomponent Multisublattice Alloys, Nonconfigurational Entropy and Other Additions to the Alloy Theoretic Automated Toolkit*, CALPHAD: Comput. Coupling Phase Diagrams Thermochem. **33**, 266 (2009).

[64] W. Humphrey, A. Dalke, and K. Schulten, *VMD-Visual Molecular Dynamics*, J. Mol. Graphics **14**, 33 (1996).

[65] A. Renninger, S. C. Moss, and B. L. Averbach, *Local Antiferromagnetic Order in Single-Crystal MnO above the Néel Temperature*, Phys. Rev. **147**, 418 (1966).

[66] I. D. Hughes, M. Däne, A. Ernst, W. Hergert, M. Lüders, J. B. Staunton, Z. Szotek, and W. M. Temmerman, *Onset of Magnetic Order in Strongly-Correlated Systems from Ab Initio Electronic Structure Calculations: Application to Transition Metal Oxides*, New J. Phys. **10**, 063010 (2008).

[67] J. A. Chan, S. Lany, and A. Zunger, *Electronic Correlation in Anion p Orbitals Impedes Ferromagnetism Due to Cation Vacancies in Zn chalcogenides*, Phys. Rev. Lett. **103**, 016404 (2009).